



Combining CFD and artificial neural network techniques to predict the thermal performance of all-glass straight evacuated tube solar collector



Bin Du ^{a, b, *}, Peter D. Lund ^{a, c}, Jun Wang ^{a, b}

^a Key Laboratory of Solar Energy Science and Technology in Jiangsu Province, Institute of Energy and Environment, Southeast University, Nanjing, 210096, China

^b Energy Storage Research Center, Southeast University, Nanjing, 210096, China

^c School of Science, Aalto University, P.O.Box 15100, FI-00076 Aalto, Espoo, Finland

ARTICLE INFO

Article history:

Received 16 July 2020

Received in revised form

28 November 2020

Accepted 24 December 2020

Available online 28 December 2020

Keywords:

Solar collector

Evacuated tube

Neural network

Multiple linear regression

CFD

Thermal performance

Prediction

ABSTRACT

Thermal performance modelling and performance prediction of a novel all-glass straight-through evacuated tube collector is analyzed here. A mathematical model of the tube was developed and incorporated into CFD software for numerical performance simulation. To improve the thermal performance prediction of the collector, different artificial neural network (ANN) models were considered. A comprehensive experimental dataset with more than 200 samples were employed for testing of the models. Integrating the thermal simulation model with the ANN models by using modelled collector output as one of the input models, significantly improved the prediction accuracy of the ANN models. The predictions based on the CFD model alone gave the poorest accuracy compared to the ANN models. The convolutional neural network (CNN) model proved to be the best ANN model in terms of prediction accuracy.

© 2021 Elsevier Ltd. All rights reserved.

1. Introduction

Renewable energy is one of the key technologies to mitigate global warming and energy access [1]. Solar energy is one of the fastest developing renewable energy sources, and it is widely used in different applications such as power generation [2], seawater desalination [3], domestic space heating [4], etc. Solar thermal applications form an important segment of solar energy utilization. The key component in such a system is the solar collector, which absorbs the solar radiation and converts it to heat, which is transferred to a heat transfer fluid [5]. Common types of solar collectors include the flat plate collector, evacuated tube collector and compound parabolic collectors [6–9], which make up most of the collector market [10,11]. Recently, the evacuated tube collector has

gained more interest due to its attractive performance and price [12–14].

An evacuated tube collector (ETC) typically contains a single-walled glass evacuated tube or a Dewar-tube [15]. The former includes a finned tube [16,17] and a U-tube [18,19], while the latter is composed of inner tube and outer tubes. The Dewar-type of evacuated tube collector dominates the market, because of its low cost and easy manufacturing [20]. The subject of this paper is a new type of ETC made of an all-glass straight vacuum tube. The heat transfer fluid at the bottom of the Dewar-tube is difficult to circulate through convection, and salt precipitating on the tube bottom hinders heat transfer and water quality will be affected on long term [21]. The main advantages of all-glass straight through evacuated tube over the standard Dewar-tube are both enhancing heat transfer and improving the water quality. A higher efficiency and performance also reduce the costs of the heat produced by the ETC and hence improve its economics.

Though the overall and optical efficiency of all-glass straight through evacuated tube collector has been found to be better than that of the traditional Dewar-type ETC [22–25], the understanding

* Corresponding author. Key Laboratory of Solar Energy Science and Technology in Jiangsu Province, Institute of Energy and Environment, Southeast University, Nanjing, 210096, China.

E-mail addresses: bindubill@hotmail.com (B. Du), peter.lund@aalto.fi (P.D. Lund), 101010980@seu.edu.cn (J. Wang).

Nomenclature			
ANN	Artificial Neural Networks	Re	Reynolds number
A	gas adaption coefficient	RMSE	root mean square error
B	gas intermolecular interaction coefficient	T	temperature (K)
BP	back propagation	W	weights
C	specific heat (J/(kg · K))	X	independent variable in MLR model
CNN	Convolutional Neural Network	Y	Dependent variable in MLR
D	diameter (m)		
D_{abs}	absorber tube diameter (m)	<i>Greek letters</i>	
DNI	direct normal solar irradiance (W/m^2)	η_{th}	thermal efficiency
F	Darcy resistance coefficient	β	undetermined coefficient in MLR
H	convective heat transfer coefficient ($W / (m^2 \cdot K)$)	ϵ	emissivity
ΔH	glass thickness (m)	δ	molecular diameter
k	thermal conductivity ($W / (m \cdot K)$)	ξ	absorptivity
L	length (m)	γ	adiabatic index
MAE	mean absolute error	λ_T	mean free distance of molecules
MLR	multiple linear regression	τ_{gla}	transmissivity of outer glass tube
MSE	mean square error		
Nu	Nusselt number	<i>Subscripts</i>	
Pa	gas pressure	a	ambient
Pr	Prandtl number	absi	inner wall of absorber tube
\dot{Q}_u	gained useful energy (W)	abs	absorber tube
Q_{loss}	energy loss (W)	f	water
R^2	coefficient of determination	gla	outer glass tube
		s	sky
		w	inner wall of absorber tube

of its thermal performance and thermal performance modelling is still incomplete. The aim of this paper is to develop a mathematical model enabling thermal simulation and performance estimates of the all-glass straight through solar vacuum tube collector. For this purpose, a thermal model of the tube accompanied by CFD software is employed. To improve the prediction accuracy of the theoretical model, it is combined with an artificial neural network which is first of its kind to our best knowledge. Such as combination of artificial intelligence (AI) and solar thermal technology presents in broad terms a new research direction.

Artificial neural network (ANN) technology has previously been applied to solar collector in different context [26–28]. For example, Delfani et al. [29] employed neural networks to investigate the performance of a solar collector with nanofluids. Ghritlahre et al. [30] used three types of neural network models to determine the performance of unidirectional flow porous bed solar air heaters. Ghritlahre et al. [31]. also utilized neural network models to estimate the heat transfer from a rough absorber plate to air passing through the ducts of solar air heater. Liu [32] et al. proposed a screening method based on machine learning to design evacuated solar water heater with high heat collection rates. Tommy et al. [33] used ANN to simulate the performance of flat plate solar collector with silver/water nanofluid showing good agreement to experimental data. ANN using surface temperature and collector parameters as input has been demonstrated [34]. Cetiner et al. [35] trained a neural network model for a solar concentrator with experimental data leading to better prediction accuracy. A range of other studies have been reported including ANN for flat plate solar collectors [36] and heat pipe solar collectors [37], or, to determine the exergy efficiency of a solar air heater [38]. Here, we will investigate the use of three different ANN models in combination with thermal modelling.

The paper starts by describing the structure of all-glass straight evacuated tube collector and the experimental set-up, which was used to verify the theoretical model and performance predications. Next, the thermal model of the tube is presented. The heat and

mass transfer equations of the tube are solved with a CFD software to yield the outlet temperature from the tube. For the artificial neural network, three different approaches are tested and their capability to predict the thermal performance of the tube is analyzed. Solar radiation intensity, ambient temperature, wind speed, collector inlet temperature and water flow rate were used as input to the ANN and the collector output temperature and thermal efficiency of the tube were the main output from the ANN. More than 200 experimental datasets were used for training and testing of the hybrid ANN-model. The results section provides a comprehensive comparison of the models against experimental data.

2. Experiment set-up

The all-glass straight through evacuated tube consists of an absorber tube (inner tube) and a cover glass tube (outer tube) shown in Fig. 1. Both ends of the inner tube and the outer tube are fused and sealed. The outer glass tube has excellent sun-light transmittance, while the outer surface of the inner glass tube is coated with solar radiation absorbing coating, meaning that the temperature of the inner tube is much higher than that of the outer glass tube when operating. Therefore, the thermal expansion values of the two tubes differ widely [6,7,9–11]. The inner glass tube is made of borosilicate glass, and the outer tube is made of glass with a higher thermal expansion coefficient, which can resist the thermal stress caused by the temperature difference. The space between the two glass layers is a vacuum. The heat transfer fluid flows through the inner tube to absorb heat. The specific structural parameters of the tube are given in Table 1 (see Fig. 2).

The experimental rig consists of the tube, supporting steel frame, pipes and connecting parts, temperature measuring instruments, flowmeter, etc. Water is used as the heat transfer medium; thermocouples are used to measure the temperature at the inlet and outlet of the tube. The sensors are connected to a data logger (Agilent 34970 A), employing a 10-min recording sequence. A rotameter is employed for the water flow rate. The flow rate range



Fig. 1. All-glass straight through solar vacuum tube.

Table 1
Technical parameters of an all-glass straight through evacuated tube.

Parameter	Value
Length, L (m)	1.8
Diameter of absorber tube, D_{abs} (m)	0.047
Diameter of outer glass tube, D_{gla} (m)	0.058
Glass thickness, ΔH (m)	0.003
Thermal conductivity of absorber tube, k_{abs} ($W / (mK)$)	1.2
Specific heat of absorber tube, C_{abs} ($J / (kg K)$)	980
Absorptivity of selective coating, ξ_{abs}	0.96
Transmissivity of outer glass tube, τ_{gla}	0.96

is stable within $\pm 1\%$. The weather parameters were measured with a small weather station. Experiments were typically done between 10 a.m. and 4 p.m. on the experimental day. The experimental site was located in Nanjing, China.

3. Thermal modelling of the tube

3.1. Energy and heat transfer equations

Most of the solar energy absorbed by the tube is transferred to the inner wall of the tube through heat conduction, and then to the fluid in the tube by heat convection. The other part of the energy is transferred to the inner wall of the outer glass tube by radiation and

convection, and then transferred through the outer glass tube by heat conduction. The outer wall of the outer glass tube loses heat to the environment by convection to the ambient air and through radiation to the sky.

Based on steady heat transfer conditions in the evacuated tube, the energy conservation equation can be written as follows [23,24]:

$$Q_{total} = Q_u + Q_{loss} \quad (1)$$

The thermal efficiency of the absorber tube is defined as:

$$\eta_{th} = \frac{Q_u}{Q_{total}} \quad (2)$$

where, Q_{total} is the total heat absorbed by the absorber tube, Q_u represents the useful heat, Q_{loss} is the energy loss. The total heat absorption can further be written as:

$$Q_{total} = L \times D_{abs} \times \xi_{abs} \times \tau_{gla} \times DNI \quad (3)$$

where L is the length of the absorber tube, D_{abs} is the diameter of the absorber tube, ξ_{abs} is the absorptivity of the selective coating on the surface of the absorber tube, τ_{gla} is the transmissivity of the outer glass tube.

The useful energy is the energy extracted by the water flow through the absorber tube and is calculated as follows [39,40]:



Fig. 2. Experimental rig.

$$Q_u = \pi D_{absi} h_f (T_{absi} - T_f) \tag{4}$$

where h_f is the convective heat transfer coefficient between the absorber tube and water, D_{absi} and T_{absi} represent the diameter and temperature of the absorber tube inner wall, T_f is the water temperature.

The convective heat transfer coefficient h_f is defined as:

$$h_f = Nu \frac{k_f}{D_{absi}} \tag{5}$$

where, k_f is the thermal conductivity of water. For the Nusselt number (Nu) applies the following relations [41–43]:

$$\text{Laminar flow, } Re < 2300, \quad Nu = 4.36 \tag{6}$$

Turbulent flow, $Re > 2300$

$$Nu = \frac{(f/8)(Re - 1000)Pr_f}{1 + 12.7\sqrt{f/8}(Pr_f^{2/3} - 1)} \left(\frac{Pr_f}{Pr_w}\right)^{0.11} \tag{7}$$

where, Pr_f is the Prandtl number at T_f , Pr_w is the Prandtl number at the inner wall temperature of the absorber tube, f represents the Darcy resistance coefficient of flowing in the circular tube, which is given by [39,40]:

$$f = 1.82[\log_{10}(Re) - 1.64]^{-2} \tag{8}$$

The heat loss from the surface of the absorber tube is described as [43–45]:

$$Q_{loss} = \pi D_{abs} \left[h_{a-g} (T_{abs} - T_{gla}) + \tau_{gla} \epsilon_{abs} \sigma (T_{abs}^4 - T_s^4) + (1 - \tau_{gla}) \frac{\sigma (T_{abs}^4 - T_{gla}^4)}{\left(1/\epsilon_{abs} + \frac{(1 - \epsilon_{gla})D_{abs}}{\epsilon_{gla}D_{gla}}\right)} \right] \tag{9}$$

where σ is the Stefan-Boltzmann constant, h_{a-g} is the heat transfer coefficient in the annular vacuum space, T_s is the sky temperature.

The wall temperature of the outer glass tube (T_{gla}) in steady state is only slightly higher than the ambient temperature [44] [-]

[45], and the heat loss can then be presented as [44,45]:

$$Q_{loss} = \pi D_{abs} h_{a-g} (T_{abs} - T_a) + \epsilon_{abs} \sigma \pi D_{abs} (T_{abs}^4 - T_s^4) \tag{10}$$

where, h_{a-g} is the convective heat transfer coefficient between absorber tube and outer glass tube, ϵ_{abs} is the emissivity of selective absorbing coating on the outer wall of the absorber tube, T_s represents the sky temperature. h_{a-g} is calculated from the following equations [43,46]:

$$h_{a-g} = \frac{k_{std}}{\frac{D_{abs}}{2 \ln\left(\frac{D_{gla}}{D_{abs}}\right)} + b \lambda_T \left(\frac{D_{gla}}{D_{abs}} + 1\right)} \tag{11}$$

$$b = \frac{(2 - a)(9\gamma_g - 5)}{2a(\gamma_g + 1)} \tag{12}$$

$$\lambda_T = \frac{2.33 \times 10^{-20} \left(\frac{T_{abs} + T_{gla}}{2} + 273.15\right)}{Pa \delta} \tag{13}$$

where, k_{std} is the thermal conductivity coefficient of gas in the annular space; δ is the molecular diameter; b represents the gas intermolecular interaction coefficient; a is the gas adaption coefficient; γ is the adiabatic index; λ_T represents the mean free distance of the molecules; Pa is the gas pressure in the annular space. The annular space between the absorber tube and the outer glass tube forms a vacuum with pressure $< 0.013 Pa$. The convective heat transfer coefficient from the absorber to the outer glass tube is $0.0001115 W/m^2 K$ [43,44].

The sky temperature is calculated by the following equation [43,47,48]:

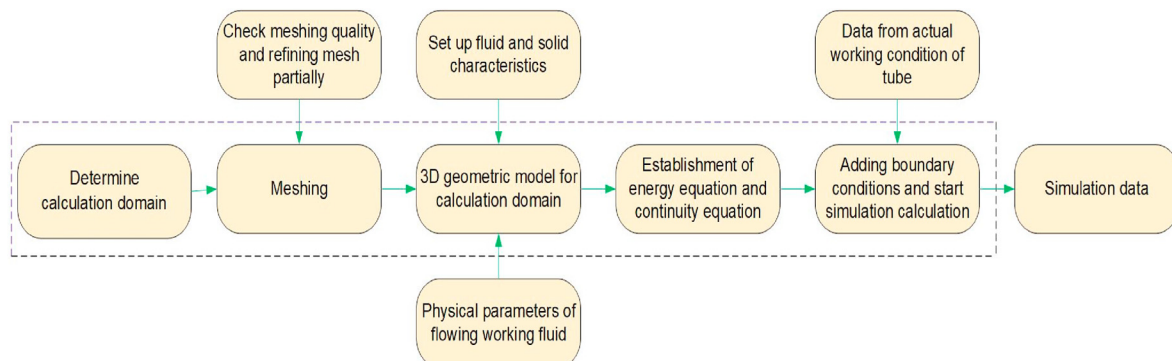


Fig. 3. Simulation flow chart.

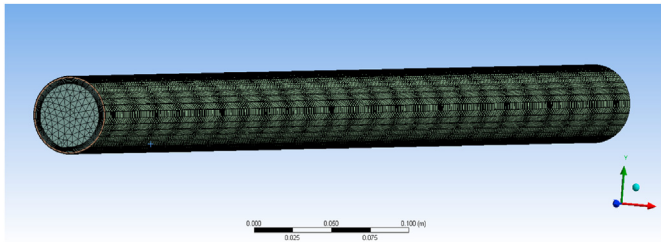


Fig. 4. Generating the mesh for the simulation of the all-glass straight-through evacuated tube collector.

$$T_s = 0.0552T_a^{\frac{3}{2}} \tag{14}$$

where, T_a is the ambient temperature.

The emissivity of the selective absorbing coating on the outer wall of absorber tube is [43,47,48]:

$$\epsilon_{abs} = 0.062 + 2 \times 10^{-7}(T_{abs} - 273.15)^2 \tag{15}$$

3.2. Numerical CFD model

The energy equations from previous section was implemented into the computational fluid dynamics (CFD) software ANSYS Fluent [49–51], but also adds all necessary mass transfer and heat and mass transfer coupling equations and boundary conditions to perform a full heat transfer analysis of the tubes. The CFD software also includes the numerical solver.

Fig. 3 illustrates the steps in the numerical simulation of the tube. The DESIGNMODELER subprogram is used to build the physical model of the tube into Fluent, followed by forming the calculation mesh of model as illustrated in Fig. 4.

In order to simplify the simulation process, several assumptions were made for the all-glass straight-through evacuated tube:

- 1) The evacuated tube is at steady-state;
- 2) The thermal contact resistance between the absorber tube wall and the working fluid is omitted;
- 3) The heat loss at the inlet and outlet of the evacuated tube is ignored;
- 4) The working fluid is incompressible and its density does not change with temperature.

The 3-D model based on the steady-state heat transfer equations

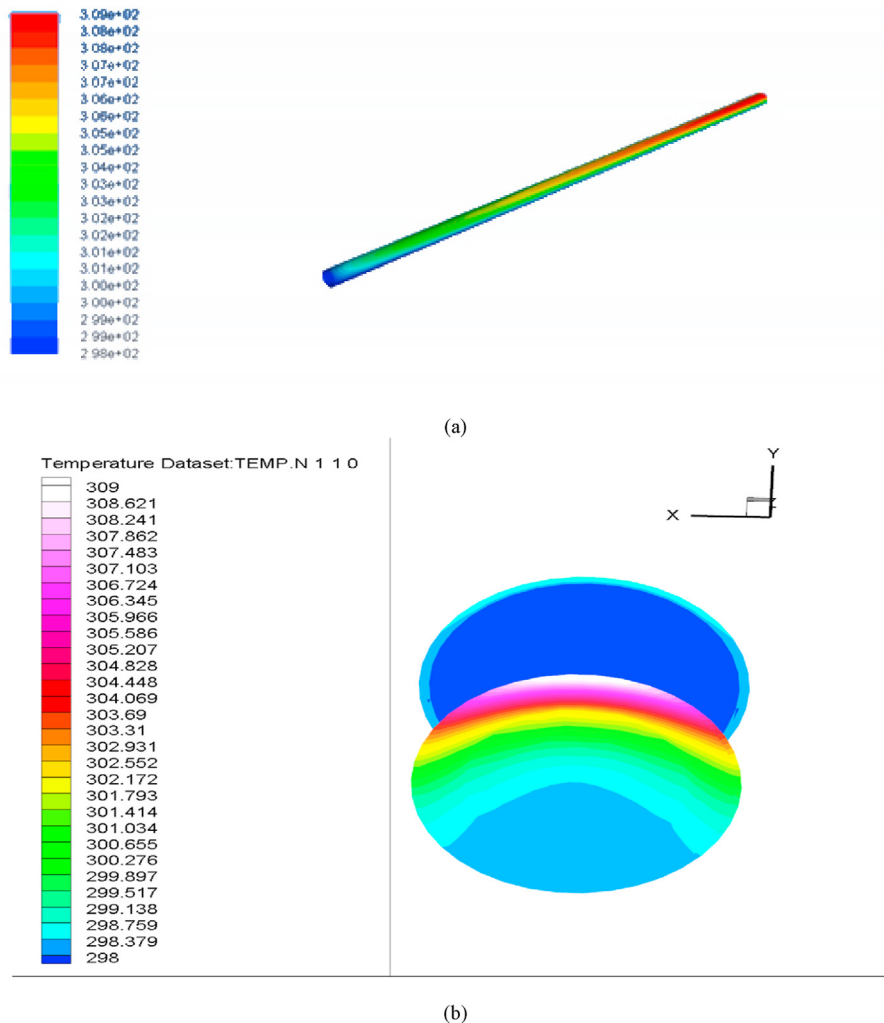
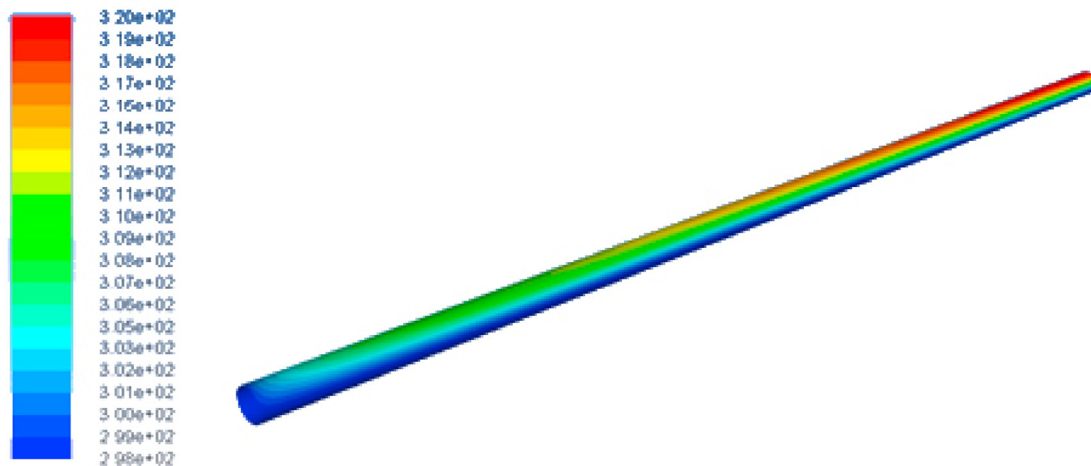
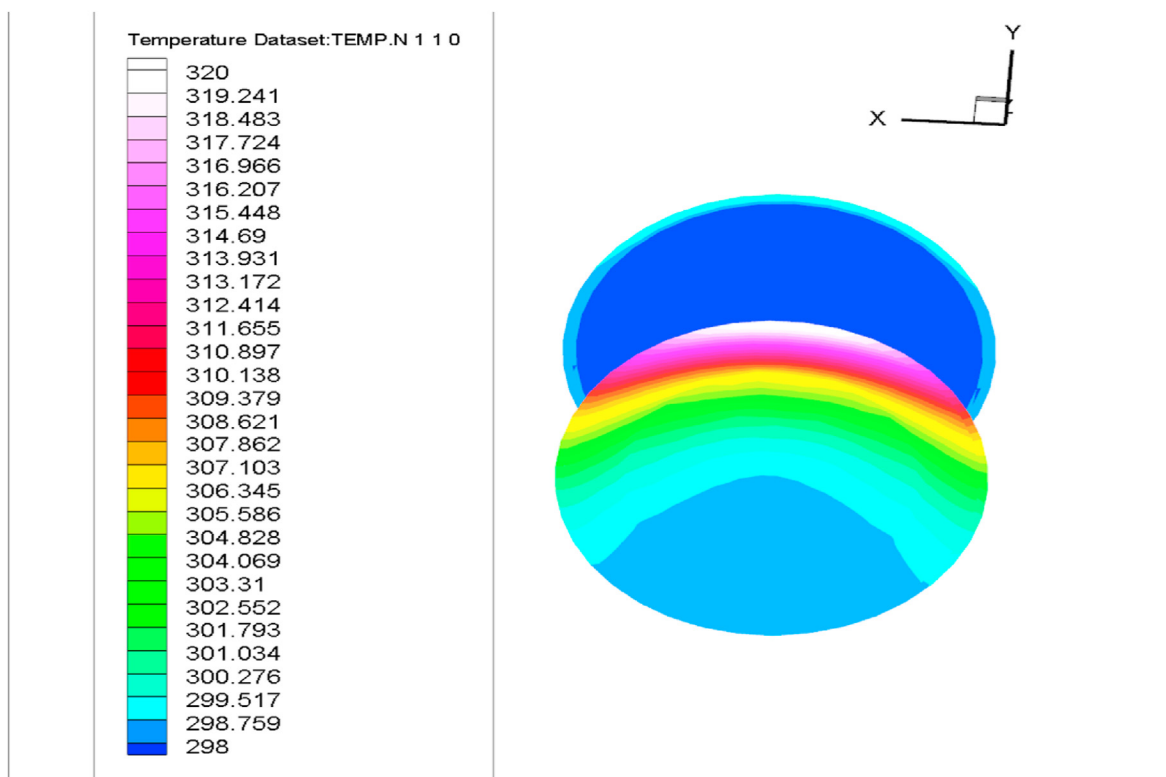


Fig. 5. (a) Temperature distribution along the tube. (b) Inlet and outlet temperature. Irradiance is 600W/m².



(a)



(b)

Fig. 6. (a) Temperature distribution along the tube. (b) Inlet and outlet temperature. Irradiance is 1000 W/m^2 .

of the all-glass straight-through evacuated tube collector is presented in Refs. [43–45] and was implemented into ANSYS Fluent computational fluid dynamics (CFD) software. A structured hexahedral mesh was generated by a meshing tool in the CFD software. The pressure and velocity were coupled by the SIMPLE algorithm. The second order upwind scheme was employed to integrate the governing equations.

Figs. 5–6 shows temperature distributions obtained through the numerical simulations using the tube model. The inlet temperature

is set to 298 K and mass flow rate to 25 kg/h. Two radiation conditions 600 W/m^2 and 1000 W/m^2 were considered. The results show that the temperature difference of the wall surface increases with the intensity. Under 600 W/m^2 irradiation, the wall temperature at the outlet end is only 309 K, while at 1000 W/m^2 irradiation, the temperature at the middle part of the wall near the inlet has reached 309 K, and the temperature at the outlet is higher than that of 600 W/m^2 case. The temperature distribution of the cylindrical tube wall is not uniform, because the heat absorption of the water

at the inlet of the tube is stronger, so the difference of the wall temperature distribution is greater and the temperature gradient is larger. It is evident that the higher the solar irradiation, the higher the average temperature at the outlet section and the higher the average temperature of the water in the tube.

4. Artificial neural network models

There are several artificial neural network (ANN) models available. As one of the most representative deep learning algorithms is the convolutional neural network (CNN), which has also been utilized in energy applications. Wang [52] et al. employed CNN, long-short term memory (LSTM) and a hybrid of these models algorithms to predict photovoltaic power generation. Their results showed that the hybrid model had the best prediction precision, followed by the convolutional neural network. For solar radiation prediction from meteorological data several data-based models have been used [53]. The K-means radial basis function(RBF) and gradient boosted regression trees (GRBT), and the CNN model had the lowest annual average error in this case. CNN based on digital mapping has been applied to estimate regional solar irradiance values [54], yielding a lower average error. CNN [55] has been used for PV fault predictions [55,56]. A LSTM-CNN hybrid model was employed to estimate photovoltaic power generation [57]. The hybrid model yields in these studies a better result than the CNN and LSTM alone.

4.1. Multiple linear regression (MLR)

Multiple linear regression is a statistical method to analyze the linear relationship between a random variable and multiple variables [58]. Multiple regression divides the variables investigated into: dependent variable defined by Y ; independent variable expressed by X_1, X_2, \dots . The main task of regression analysis is to determine the relationship between independent variable and dependent variable: (1) to solve the parameters of a model based on the measured data; (2) to evaluate whether the regression model fits the actual data well; (3) to implement prediction using the model.

The model is set as:

$$Y_i = \beta_0 + \beta_1 X_1 + \beta_2 X_2 + \dots + \beta_p X_p + \varepsilon_i \quad (16)$$

N groups of independently observed sample data are substituted into [Eq. 16]:

$$(y_i, x_{i1}, x_{i2}, \dots, x_{ip}) \quad i = 1, 2, \dots, n \quad (17)$$

$$y_i = b_0 + b_1 x_{i1} + b_2 x_{i2} + \dots + b_p x_{ip} + e_i \quad (18)$$

Let $\sum (e_i)^2 = \min$, to compute the estimated value of β_0, \dots, β_p , that is: b_0, \dots, b_p .

The regression equation is expressed as:

$$\hat{y}_i = b_0 + b_1 x_{i1} + b_2 x_{i2} + \dots + b_p x_{ip} \quad (19)$$

To introduce [Eq. 19] into $\sum (Y - \hat{Y})^2$, by solving partial derivative of $b_0, b_1, b_2, \dots, b_p$, the equations acquired,

$$x'(y - xb) = 0 \quad (20)$$

$$b = (x'x)^{-1} x'y \quad (21)$$

4.2. Back propagation network

The back propagation (BP) neural network, i.e. the learning process of the error back-propagation algorithm, consists of two processes: forward propagation of information and back-propagation of error [59,60], as shown in Fig. 7.

The neurons in the input layer are responsible for receiving input information from the outside and transmitting them to the neurons in the middle layer. The middle layer is the internal information processing layer, whose duty is information transformation. According to the requirements of the information variation capability, the middle layer can be designed as a single hidden layer or multiple hidden layer structure. As illustrated in Fig. 7, for the i th neuron, x_1, x_2, \dots, x_j are the inputs of the neuron, these inputs are independent variables that have a key impact on the system model, and w_1, w_2, \dots, w_j are the connection weights to adjust the weight ratio of each input.

The last hidden layer transmits the information to each neuron in the output layer. After further processing, it completes a learning forward propagation process, and outputs the information processing results from the output layer to the outside.

When the actual output is not consistent with the expected output, the error back-propagation phase is activated. Through the output layer, the weight of each layer is corrected according to the error gradient descent, and the error is transmitted back layer by layer to the hidden layer and to the input layer. The process of the

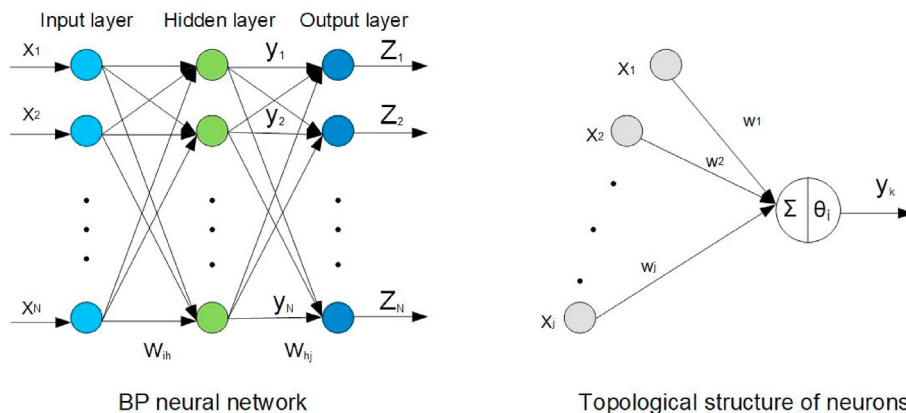


Fig. 7. BP neural network.

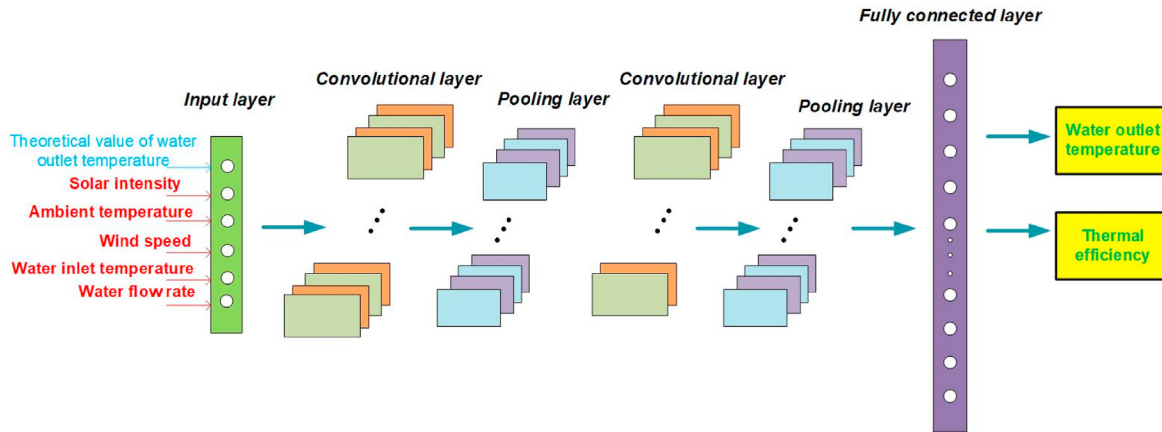


Fig. 8. Flow chart of the CNN model.

information forward propagation and error back-propagation is a process of adjusting the weights of each layer. It is also the central process of the neural network learning and training. This process continues until the error of the network output is reduced to an acceptable level or the number of learning times is set in advance.

4.3. Convolutional neural network

The hidden layer of convolutional neural network includes a convolution layer, pooling layer and full connection layer [61,62]. The structure of the CNN model is illustrated in Fig. 8.

The convolution layer is in charge of the feature extraction of input data. It contains several convolution kernels. Each element of the convolution kernel corresponds to a weight coefficient kernel and a bias vector, which is similar to the neuron of a feedforward neural network. Each neuron in the convolution layer is connected with several neurons in the region close to each other in the previous layer. The size of the region depends on the size of the convolution kernel, also known as the “receptive field”. When the convolution kernel works, it will scan the input features regularly, multiple the input features in the receptive field and add the deviation.

Convolution layer parameters contain the convolution kernel size, step size and filling. The larger the convolution kernel is, the more complex the extracted input features are. The convolution step size defines the distance between the positions of the convolution kernel when it scans the feature image twice. Filling is a method to increase the size of the feature image by convolution kernel to counteract the effect of size shrinkage before the feature graph passes through the convolution kernel. The convolution layer contains an activation function to help express complex features.

After feature extraction in the convolution layer, the output feature map will be transferred to the pooling layer for feature selection and information filtering. The selection of pooling area in pooling layer is the same as that of convolution kernel scanning feature map, which is controlled by pool size, step size and filling.

The fully connected layer is located in the last part of convolutional neural network, and only transmits signals to other fully connected layers. The convolution layer and pooling layer in the convolutional neural network extract the features of the input data. The function of the fully connection layer is to nonlinear combine the features of the extracted features to get the output, that is, the fully connection layer tries to use the existing high-order features to complete the learning goal.

A 1-dimensional convolutional neural network is chosen in this

present study to implement prediction.

4.4. Normalization

Normalization is a basic function of data mining. Different evaluation indexes often have different dimensions and dimensional units, which will affect the results of the data analysis [5]. In order to eliminate the dimensional influence between the indicators, data standardization processing is needed to solve the comparability between data indicators. After the standardization of the original data, each index is in the same order of magnitude, which is suitable for comprehensive comparative evaluation.

The data normalization equation is given as:

$$Y_{norm} = \frac{Y_i - mean}{std} \quad (22)$$

where, mean is the average of training data, std represents the standard deviation of data.

4.5. Performance evaluation indicators

Root mean square error (RMSE), mean absolute error (MAE) and coefficient of determination (R^2) [63] [64] are employed to evaluate the prediction accuracy of the three models. These are defined as follows:

Coefficient of Determination:

$$R^2 = 1 - \frac{\sum_{i=1}^n (X_{A,i} - X_{P,i})^2}{\sum_{i=1}^n X_{P,i}^2} \quad (23)$$

Root Mean Square Error:

$$RMSE = \sqrt{\frac{1}{n} \sum_{i=1}^n (X_{A,i} - X_{P,i})^2} \quad (24)$$

Mean Absolute Error:

$$MAE = \frac{1}{n} \sum_{i=1}^n (X_{A,i} - X_{P,i}) \quad (25)$$

ANN model integrated with CFD

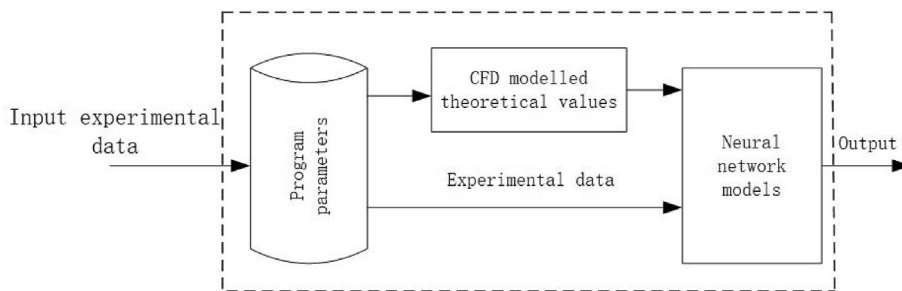


Fig. 9. Flow chart of the integrated models.

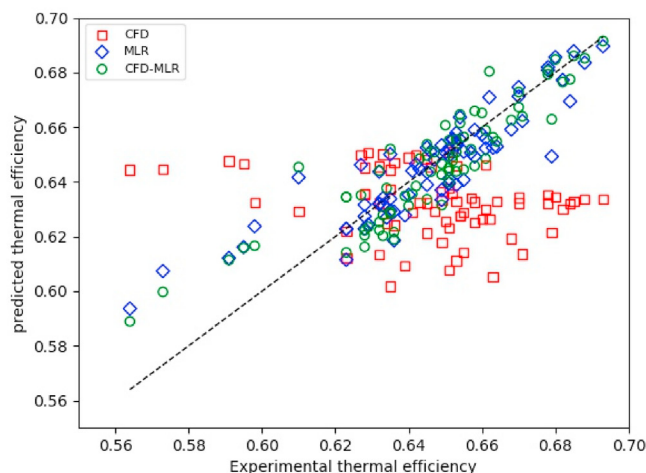
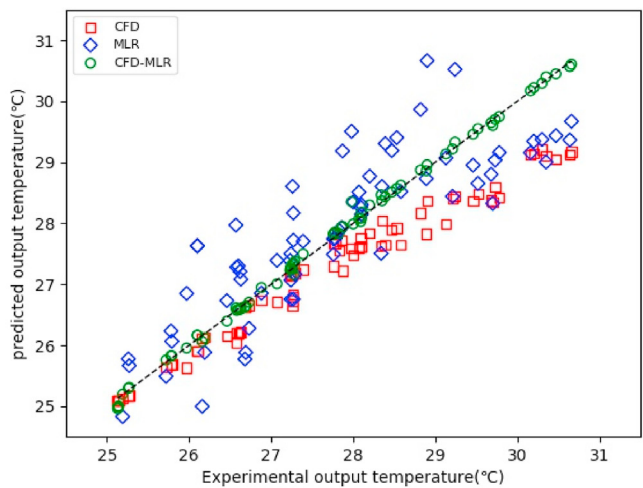
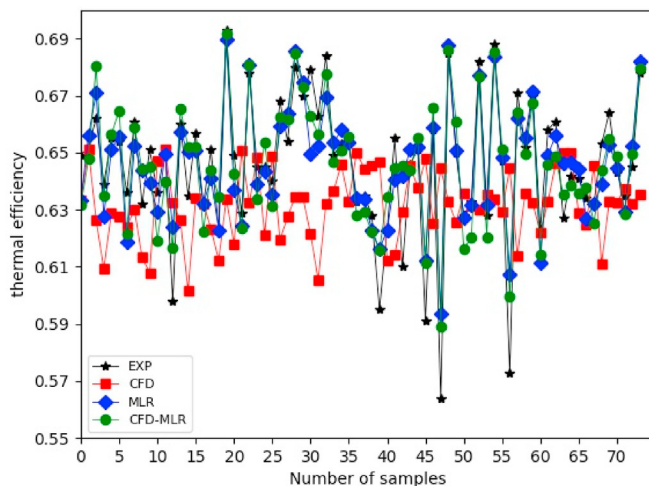
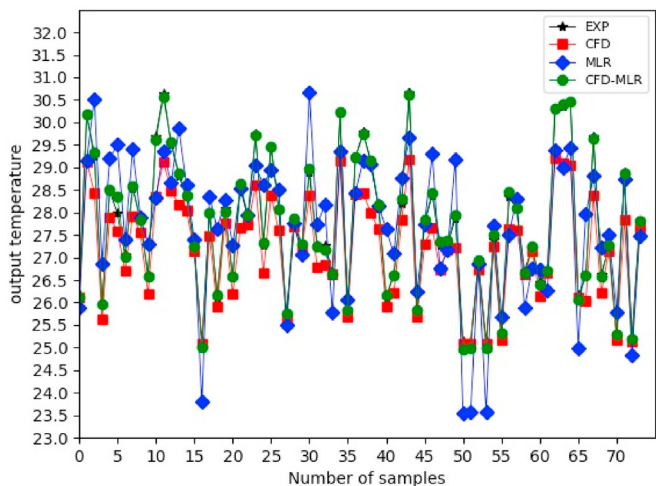


Fig. 10. Comparison of experimental and modelled collector outlet temperature with CFD, MLR and CFD-MLR.

Fig. 11. Comparison of experimental and modelled collector thermal efficiency with CFD, MLR and CFD-MLR.

5. Results and discussion

The MLR, BP and CNN models were utilized to predict the thermal performance of all-glass straight through solar vacuum tube. During the experiment, the range of water flow rate was from 20 L/h to 250 L/h, the inlet water temperature was between 25 °C and 27 °C, and the meteorological parameters were recorded in

real-time. 243 experimental datasets in total were used, 70% of which were adopted for training and 30% for the test. The specific training and test procedure was the following:

- 1) A set of hyperparameters of the model is selected, e.g. the neuron number in the hidden layer of the neural network;

- 2) Training data is divided into a training set and a validation set. The training set is adopted to train the model, and then the cross-validation set is employed to measure the performance of the model;
- 3) The hyperparameters of this model are changed and step 2) is repeated until all the hyperparameter combinations have been tested and verified;
- 4) The model with the smallest error (validation set) is selected and trained using the whole training data set;
- 5) In the test data set, the generalization performance of the optimal model obtained by the above steps is measured.

For cross-validation, the training data set is divided into k sets, each time $k-1$ sets are used as the training data and the other one is adopted as the validation data. For each model, the algorithm is executed k times. The average error value obtained from the k -times executions is taken as the error of the model.

Based on the experimental data, the CFD software and thermal modes were used to calculate the outlet temperature and the thermal efficiency of the tube (see Fig. 9). The solar radiation intensity, ambient temperature, tube inlet temperature, water flow rate, wind speed and the theoretical values calculated by the

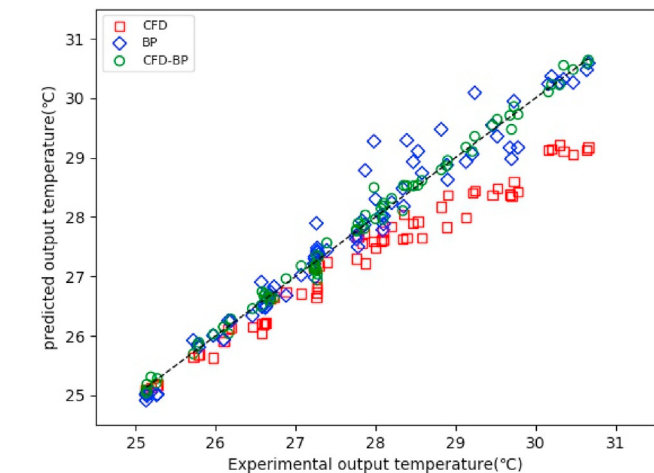
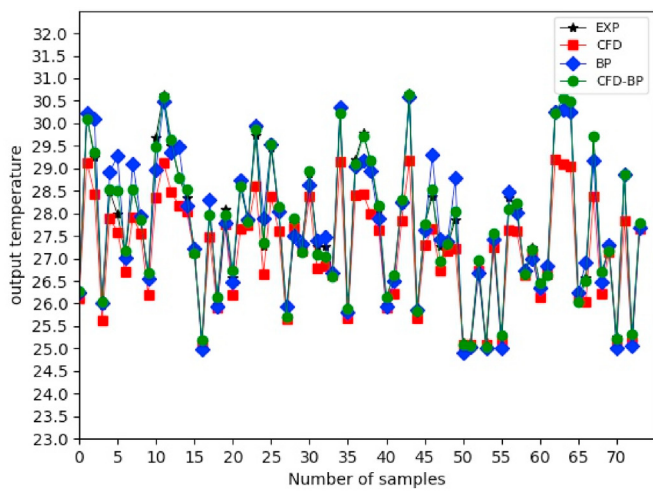


Fig. 12. Comparison of experimental and modelled collector outlet temperature with CFD, BP and CFD-BP.

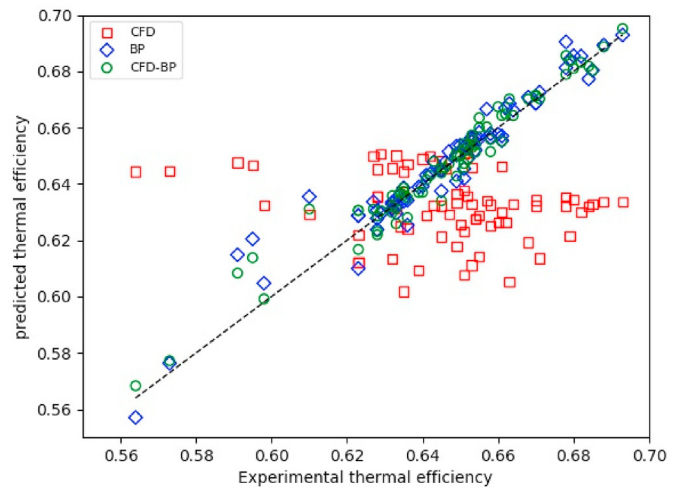
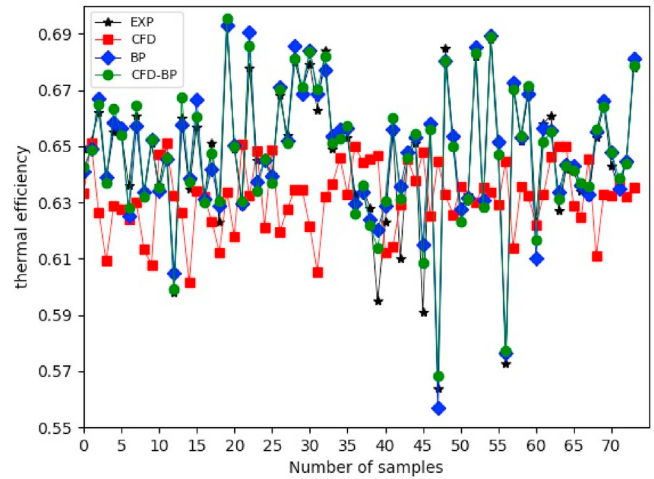


Fig. 13. Comparison of experimental and modelled collector thermal efficiency with CFD, BP and CFD-BP.

models were selected as input parameters for the ANN models. The water outlet temperature and the thermal efficiency of the solar vacuum tube obtained with and without using the thermal model + CFD were then compared to experimental results.

5.1. MLR model

The prediction results of the MLR model are shown in Figs. 10–11. When the simulated value of the tube outlet temperature was not included as an input parameter, the maximum forecast error of the outlet temperature reached 1.8 °C and the maximum error of thermal efficiency reaches 0.034. Whereas when the simulated outlet temperature was combined with the MLR model, the difference between the predicted and actual data dropped to 0.4 °C and 0.025 respectively. However, the error in the modelled and measured thermal efficiency is still relatively large.

5.2. BP model

A hidden layer based on the Relu [52] function was adopted in the BP model and a linear function was utilized for the output layer:

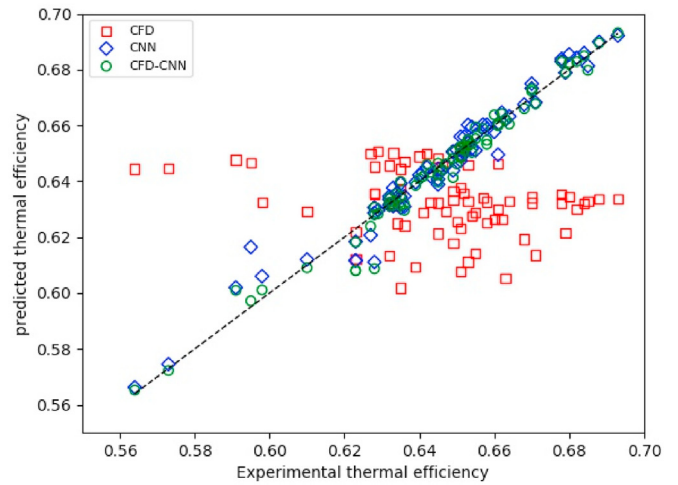
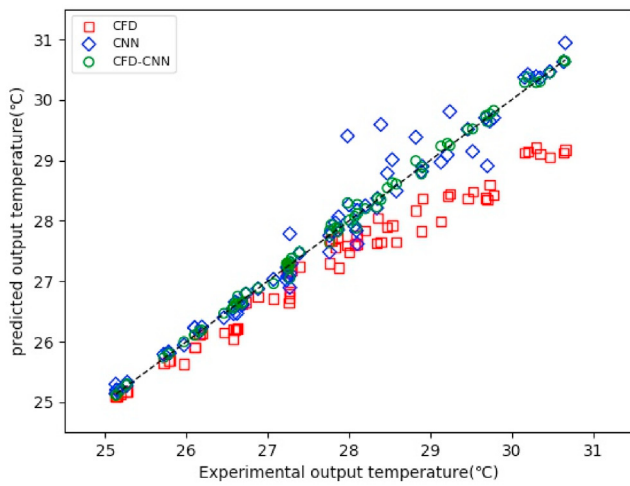
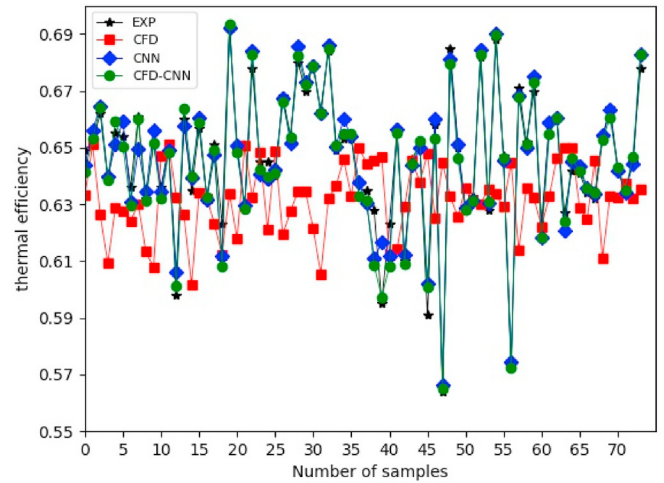
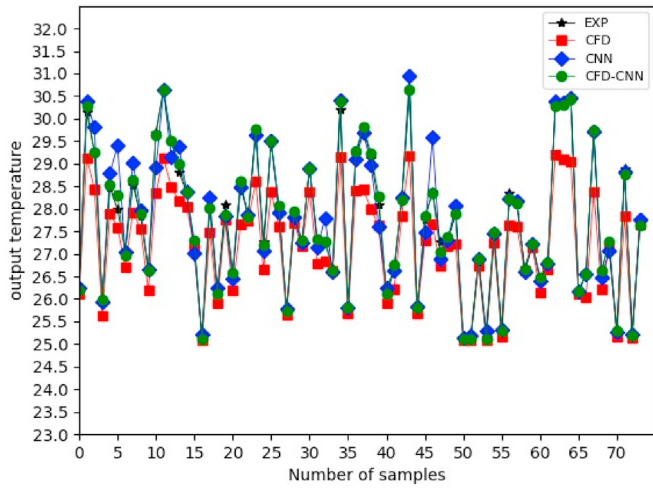


Fig. 14. Comparison of experimental and modelled collector outlet temperature with CFD, CNN and CFD-CNN.

Fig. 15. Comparison of experimental and modelled collector thermal efficiency with CFD, CNN and CFD-CNN.

$$\text{Relu}(x) = \max\{0, x\} = \begin{cases} x & \text{if } x \geq 0 \\ 0 & \text{if } x < 0 \end{cases} \quad (26)$$

The linear function is the activation function in which the output is proportional to the input [65]:

$$\psi(v_k) = cv_k \quad (27)$$

where, c is the slope of the output of the function.

The number of neurons in the hidden layer was chosen as follows [26]:

$$H = \left(\frac{I+O}{2}\right) + \sqrt{T} \quad (28)$$

where I and O are the number of input and output parameters, T represents the number of training datasets, which gave 16 as the number of neurons in the hidden layer.

It can be seen from Figs. 12–13 that when the meteorological data, collector inlet temperature and flow rate only are used in the input layer of the model, the prediction accuracy of the BP method is better than that of the mathematical models. The mathematical

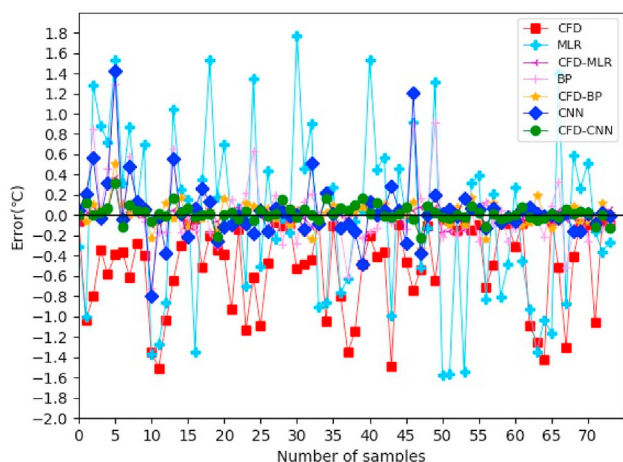
models are established on the basis of many simplifying assumptions, which results in errors in the simulation results of mathematical models, which in turn leads to reduced model accuracy [65]. Moreover, the performance of an evacuated tube is affected by several factors, for which reason it is often difficult to precisely predict the performance with simplified mathematical models. When the simulated value of collector outlet temperature is added into the input vector, the difference between the BP network (case CFD-BP) and the experimental data is further reduced and the forecast accuracy is improved.

5.3. CNN model

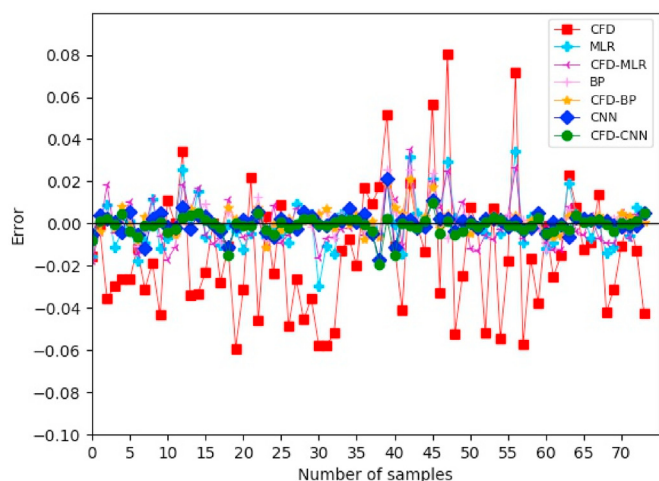
A 1-dimensional convolution neural network is employed here. In the first convolution, the number of filters is 32 and the kernel size is 3. In the second convolution, 64 filters are used and the kernel size is 3. The Relu function is employed as the activation function in the convolution, and a linear function is used in the output layer. The predicted values by the CNN model are compared with the experimental data in Figs. 14–15. Most of the deviations in the collector outlet temperature is within 0.6 °C. The error of the tube thermal efficiency is between -0.016 and 0.021. When the

Table 2
Inaccuracies of the different models.

Models	R^2		RMSE		MAE	
	Water outlet temperature	Thermal efficiency	Water outlet temperature(°C)	Thermal efficiency	Water outlet temperature(°C)	Thermal efficiency
CFD-CNN	0.9971	0.9684	0.0823	0.0044	0.0559	0.0028
CNN	0.9629	0.9548	0.3002	0.0051	0.1693	0.0036
CFD-BP	0.9937	0.9434	0.1209	0.0055	0.0910	0.0038
BP	0.9555	0.9192	0.3305	0.0067	0.2219	0.0043
CFD-MLR	0.9924	0.7443	0.0975	0.0108	0.0564	0.0086
MLR	0.7210	0.6736	0.8436	0.0112	0.6920	0.0080



(a)



(b)

Fig. 16. Prediction error of collector (a) outlet temperature and (b) thermal efficiency by the models.

theoretical modelled collector outlet temperature is used as one of the input parameters, the forecast performance of CNN is improved, the deviations in the collector outlet temperature is decreased to 0.2 °C. The error between the thermal efficiency of the tube by the CNN model and the actual data is reduced to 0.007. This clearly emphasizes the importance of the modelled collector outlet temperature as input parameter in the CNN method to improve

prediction accuracy.

5.4. Comparison of prediction performance of different models

The prediction accuracies of the MLR, BP and CNN models are summarized in Table 2. The CNN model using the modelled value as one of the input parameters (CFD-CNN) obtained the best R^2 and the lowest RMSE. When predicting the thermal efficiency of the tube, the forecast precision of the CNN method without the CFD input (CNN) is slightly better than that of the BP model with the CFD (BP-CFD). Based on the comparison in Table 2, the prediction accuracy of the MLR, BP and CNN models are clearly improved when the modelled value of the collector outlet temperature is added in the input layer.

The forecast results by the MLR, BP and CNN models are compared with the experimental data for each sample in Fig. 16, which confirms the improvement of the prediction accuracy of the different models when adding the modelled value of collector outlet temperature in the input. The performance of the CNN and BP models in terms of the collector outlet temperature and thermal efficiency prediction is clearly better than that of the modelled values using the CFD software on the basis of mathematical model.

According to the above comparison, the CFD-CNN model appears the best followed by the BP model, both of which are better than the MLR and CFD alone.

Statistical results available from the present literature are shown in Table 3. Comparing Table 3 to the results of the present work, the CFD-CNN and CFD-BP models of the present study perform well and their prediction accuracy is often higher than that of several other studies in the past.

6. Conclusion

In this paper, the thermal performance modelling and performance prediction of an all-glass straight through evacuated tube collector has been investigated. This new type of ETC has many benefits over the traditional Dewar-type of ETC [6,8,9,12–15,19,21–25,45,74]. A mathematical model of the all glass straight through evacuated tube was developed and incorporated into CFD software for numerical performance simulation. To improve the thermal performance prediction of the collector, different artificial neural network models were analyzed. A comprehensive experimental dataset with more than 200 samples were employed for testing of the models.

The results show that integrating the modelled collector outlet temperature as input to the ANN models clearly improves their prediction accuracy of all models considered (MLR, BP and CNN). The collector outlet temperature and thermal efficiency were used in the comparison, and the accuracy of these both parameters were improved. Solar radiation intensity, ambient temperature, wind speed, water flow rate, and collector inlet temperature were used as input in these analyses [30,35,37,38,72,73]. The predictions based

Table 3
Summary of prediction accuracy of solar collector performance found in the literature.

Authors	Model type	Outlet temperature of heat transfer fluid		Thermal efficiency		
		RMSE(°C)	R ²	RMSE	R ²	
Caner et al. [66]	MLP			0.0173 _{avg}	0.997 _{avg}	
	MLR			0.0649	0.875	
Benli [67]	MLP			0.0575 _{avg}	0.9919 _{avg}	
Dickmen et al. [30,68]	MLP			0.04763	0.81191	
	ANFIS			0.06196	0.68167	
Shafieian et al. [37]	Spring	ANN		0.00720	0.98079	
		ANFIS		0.00335	0.86222	
		TRN		0.24826	0.8674	
	Summer	ANN		0.00525	0.98974	
		ANFIS		0.00461	0.94201	
		TRN		0.21473	0.89965	
	Autumn	ANN		0.01348	0.98903	
		ANFIS		0.02553	0.95493	
		TRN		0.33123	0.85703	
	Winter	ANN		0.00531	0.99209	
		ANFIS		0.02376	0.95547	
		TRN		0.32865	0.87684	
H. Esen et al. [69]	WNN	0.05 kg/s air flow rate	0.0058	0.9989	0.0126	0.9992
		0.03 kg/s air flow rate	0.0034	0.9994	0.0094	0.9992
Xie et al. [5,70]	MLP			0.0075	0.9999	
Y. Varol et al. [71]	ANN				0.844–0.872	
	ANFIS				0.879–0.905	
H.K. Ghritlahre et al. [72]	MLP	0.39699	0.9864	0.01079	0.93537	
F.J. Diez et al. [73]	MLP	0.0090	0.7443			
Present work	CFD-CNN	0.0823	0.9971	0.0044	0.9684	
	CNN	0.3002	0.9629	0.0051	0.9548	
	CFD-BP	0.1209	0.9937	0.0055	0.9434	
	BP	0.3305	0.9555	0.0067	0.9192	
	CFD-MLR	0.0975	0.9924	0.0108	0.7443	
	MLR	0.8436	0.7210	0.0112	0.6736	

on the CFD model alone gave the poorest accuracy compared to MLR, BP and CNN methods. The main reason for this is the simplifying assumptions used for modelling the ETC, also the difficulty to account for the many factors affecting the performance of the evacuated tube. Whereas the neural networks can deal with nonlinear problems [75].

The performance results using BP and CNN methods are better than those obtained by the MLR model, as MLR is not that good in dealing with nonlinear problems. For example, for the thermal efficiency prediction, the R² of MLR is 43.8% lower and the RMSE is 54.5% higher than with CNN. The CNN model is slightly better than the BP model and both of them are better than the MLR and CFD models. The traditional BP algorithm has too many weights and needs a large amount of calculation, whereas the CNN is less complex through the receptive field and weight sharing technique, which also improves the model performance.

The CFD-CNN model is the most optimal one among the studied models to determine the thermal efficiency of the evacuated tube, due to lowest RMSE (0.0044), lowest MAE (0.0028) and highest value of R² (0.9684). The same applies to the water outlet temperature prediction. In overall, the prediction performance of the models significantly improved by combining the CFD model and ANN techniques. The accuracy of the model was improved through the learning function of the neural network, i.e. the model is corrected by the learning deviation between the calculated value from the mathematical model and the measured data. As the training process of the neural network aims at minimizing the difference between the calculated and the measured value, combining the CFD and the neural network model yield a better prediction.

Future research work may focus on using new types of ANNs such as recurrent neural networks for performance prediction of solar thermal energy application systems, and to compare the

accuracy with traditional models. To utilize metaheuristic methods, for example, particle swarm optimization (PSO), genetic algorithms (GA), grey wolf optimization (GWO), to optimize the ANN structure and thus improve the performance of ANNs would also be relevant for future work. Extensions of ANNs, e.g. Adaptive Network-based Fuzzy Inference System, extreme machine learning (EML) etc., usually have a high quality, and applying them for performance predictions would be interesting.

Credit author statement

Bin Du: Conceptualization, Formal analysis, Writing – original draft. Peter D.Lund: Writing – review & editing. Jun Wang: Supervision, Project administration.

Declaration of competing interest

The authors declare that they have no known competing financial interests or personal relationships that could have appeared to influence the work reported in this paper.

Acknowledgements

The work was funded by the National Science Foundation of China (Grant number 51736006). The support of Aalto University is also acknowledged.

References

[1] Guven G, Sulun Y. Pre-service teacher's knowledge and awareness about renewable energy. *Renew Sustain Energy Rev* 2017;80(12):663–8.
 [2] Jain S, Kumar Jain N, Jamie Vaughn W. Challenges in meeting all of India's electricity from solar: an energetic approach. *Renew Sustain Energy Rev*

- 2018;82(2):1006–13. part 1.
- [3] Sharshir SW, Yang Nuo, Peng Guilong, Kabeel AE. Factors affecting solar stills productivity and improvement techniques: a detailed review. *Appl Therm Eng* 2016;100(5):267–84.
 - [4] Sharma AK, Sharma C, Mullick SC, Kandpal TC. Solar industrial process heating: a review. *Renew Sustain Energy Rev* 2017;78(10):124–37.
 - [5] Ghritlahre HK, Prasad RK. Application of ANN technique to predict the performance of solar collector systems- A review. *Renew Sustain Energy Rev* 2018;84(3):75–88.
 - [6] Mathioulakis EE, Christodoulidou MC, Papanicolaou EL, Belessiotis VG. Energetic performance assessment of solar water heating systems in the context of their energy labeling. *Renew Energy* 2017;113(12):554–62.
 - [7] Jamar A, Majid ZAA, Azmi WH, Norhafana M, ARazak A. A review of water heating system for solar energy application. *Int Commun Heat Mass Tran* 2016;76(8):178–87.
 - [8] Pater S. Field measurements and energy performance analysis of renewable energy source devices in a heating and cooling system in a residential building in southern Poland. *Energy Build* 2019;199(9):115–25.
 - [9] Suman S, Kaleem M, Pathak M. Performance enhancement of solar collectors- A review. *Renew Sustain Energy Rev* 2015;49(9):192–210.
 - [10] Shukla R, Sumathy K, Erickson P, Gong Jiawei. Recent advances in the solar water heating systems: a review. *Renew Sustain Energy Rev* 2013;19(3):173–90.
 - [11] Sabiha MA, Saidur R, mekhilef S, mahian O. Progress and latest developments of evacuated tube solar collectors. *Renew Sustain Energy Rev* 2015;51(11):1038–54.
 - [12] Barbosa EG, de Araujo MEV, de Moraes MJ, Martins MA. Influence of the absorber tubes configuration on the performance of low cost solar water heating systems. *J Clean Prod* 2019;222(6):2–8.
 - [13] Esen M, Esen H. Experimental investigation of a two-phase closed thermo-siphon solar water heater. *Sol Energy* 2005;79(11):459–68. Issue 5.
 - [14] Allouhi A, Benzakour Amine M, Buker MS, Kousksou T, Jamil A. Forced-circulation solar water heating system using het pipe-flat plate collectors: energy and exergy analysis. *Energy* 2019;180(8):429–43.
 - [15] Kim Y, Seo T. Thermal performances comparisons of the glass evacuated tube collectors with shapes of absorber tube. *Renew Energy* 2007;32(4):772–95. Issue 5.
 - [16] Ayompe LM, Duffy A. Thermal performance analysis of a solar water heating system with heat pipe evacuated tube collector using data from a field trial. *Sol Energy* 2013;90(4):17–28.
 - [17] Esen M. Thermal performance of a solar cooker integrated vacuum-tube collector with heat pipes containing different refrigerants. *Sol Energy* 2004;76:751–7. Issue 6.
 - [18] Daghigh R, Shafieian A. Theoretical and experimental analysis of thermal performance of a solar water heating system with evacuated tube heat pipe collector. *Appl Therm Eng* 2016;103(6):1219–27.
 - [19] Gao Y, Zhang QL, Fan R, Lin Xx, Yu Y. Effects of thermal mass and flow rate on forced-circulation solar hot-water system: comparison of water-in-glass and U-pipe evacuated-tube solar collectors. *Sol Energy* 2013;98(12):290–301. Part C.
 - [20] Qiu Shf, Ruth M, Ghosh S. Evacuated tube collectors: a notable driver behind the solar water heater industry in China. *Renew Sustain Energy Rev* 2015;47(7):580–8.
 - [21] Salgado-Conrado L, Areliu Lopez-Montelongo, Barriers and solutions of solar water heaters in Mexican household. *Sol Energy* 2019;188(8):831–8.
 - [22] Li Jr, Li Xd, Wang Y, Tu Jy. A theoretical model of natural circulation flow and heat transfer within horizontal evacuated tube considering the secondary flow. *Renew Energy* 2020;147(3):630–8. Part 1.
 - [23] Sobhansarbandi S, Martinez PM, Papadimitratos A, Zakhidov A, Hassanipour F. Evacuated tube solar collector with multifunctional absorber layers. *Sol Energy* 2017;146(4):342–50.
 - [24] Budihardjo I, Morrison GL, Behnia M. Natural circulation flow through water-in-glass evacuated tube solar collectors. *Sol Energy* 2007;81(12):1460–72. Issue 12.
 - [25] Morrison GL, Budihardjo I, Behnia M. Measurement and simulation of flow rate in a water-in-glass evacuated tube solar water heater. *Sol Energy* 2005;78(2):257–67. Issue 2.
 - [26] A Kalogirou S. Artificial neural networks in renewable energy systems applications: a review. *Renew Sustain Energy Rev* 2001;5(12):373–401. Issue 4.
 - [27] Bou-Rabee M, Sulaiman SA, Saleh MS, Maraf S. Using artificial neural networks to estimate solar radiation in Kuwait. *Renew Sustain Energy Rev* 2017;72(5):434–8.
 - [28] Ferlito S, Adinolfi G, Graditi G. Comparative analysis of data-driven methods online and offline trained to the forecasting of grid-connected photovoltaic plant production. *Appl Energy* 2017;205(11):116–29.
 - [29] Delfani S, Esmaeili M, Karami M. Application of artificial neural network for performance prediction of a nanofluid-based direct absorption solar collector. *Sustainable Energy Technologies and Assessment* 2019;36(12):1–11.
 - [30] Ghritlahre HK, Prasad RK. Investigation of thermal performance of unidirectional flow porous bed solar air heater using MLP, GRNN, and RBF models of ANN technique. *Thermal Science and Engineering Progress* 2018;6(6):226–35.
 - [31] Ghritlahre HK, Prasad RK. Prediction of heat transfer of two different types of roughened solar air heater using Artificial Neural Network technique. *Thermal Science and Engineering Progress* 2018;8(12):145–53.
 - [32] Liu Zhj, Li Hao, Liu KJ, Yu hch, Cheng Kw. Design of high-performance water-in-glass evacuated tube solar water heaters by a high-throughput screening based on machine learning: a combined modeling and experimental study. *Sol Energy* 2017;142(1):61–7.
 - [33] Tomy AM, Ahammed N, Subathra MSP, Asirvatham LG. Analysing the performance of a flat plate solar collector with silver/water nanofluid using artificial neural network. *Procedia Computer Science* 2016;93:33–40.
 - [34] Sozen A, Menlik T, Unvar S. Determination of efficiency of flat-plate solar collectors using neural network approach. *Expert Syst Appl* 2008;35(11):1553–1539.
 - [35] Cetiner C, Halici F, Cacur H, Taymaz I. Generating hot water by solar energy and application of neural network. *Appl Therm Eng* 2005;25(6):1337–48.
 - [36] Kalogirou SA. Prediction of flat-plate collector performance parameters using artificial neural networks. *Sol Energy* 2006;80(3):248–59.
 - [37] Shafieian A, Parastvand H, Khadani M. Comparative and performative investigation of various data-based and conventional theoretical methods for modelling heat pipe solar collectors. *Sol Energy* 2020;198(3):212–23.
 - [38] Ghritlahre HK, Prasad RK. Exergetic performance prediction of solar air heater using MLP, GRNN and RBF models of artificial neural network technique. *J Environ Manag* 2018;223(10):566–75.
 - [39] Cengel YA. Heat transfer and mass transfer: a practical approach. third ed. McGraw Hill Book Company; 2006.
 - [40] Tao WQ. Numerical heat transfer. second ed. Xi'an: Xi'an Jiaotong University Press; 2001.
 - [41] Allouhi A, Benzakour Amine M, Buker MS, Kousksou T, Jamil A. Forced-circulation solar water heating system using heat pipe-flat plate collectors: energy and exergy analysis. *Energy* 2019;180(8):429–43.
 - [42] Kim Y, Seo T. Thermal performances comparisons of the glass evacuated tube solar collectors with shapes of absorber tube. *Renew Energy* 2007;32(4):772–95. Issue 5.
 - [43] Gong Jh, Wang J, Lund PD, Hu En-yi, Xu Zhch, Liu Gp, Li Gsh. Improving the performance of a 2-stage large aperture parabolic trough solar concentrator using a secondary reflector designed by adaptive method. *Renew Energy* 2020;152(6):23–33.
 - [44] Gong Jh, Wang J, Lund PD, Zhao Dd, Hu En-yi, Jin W. Improving the performance of large-aperture parabolic trough solar concentrator using semi-circular absorber tube with external fin and flat-plate radiation shield. *Renew Energy* 2010;159(10):1215–23.
 - [45] Gong Jh, Jiang Zh, Luo Xf, Du B, Wang J, Lund PD. Straight-through all-glass evacuated tube solar collector for low and medium temperature applications. *Sol Energy* 2020;201(5):935–43.
 - [46] Kearney D, Herrmann U, Nava P. Assessment of a molten salt heat transfer fluid in a parabolic trough solar field. *Journal of solar energy engineering-Transaction of the ASME* 2003;125(2):170–6.
 - [47] Mwesigye A, Meyer JP. Optimal thermal and thermodynamic performance of a solar parabolic trough receiver with different nanofluids and at different concentration ratios. *Appl Energy* 2017;193(5):393–413.
 - [48] Qiu Y, He YL, Cheng ZD, Wang K. Study on optical and thermal performance of a linear Fresnel solar reflector using molten salt as HTF with MCRT and FVM methods. *Appl Energy* 2015;146(5):162–73.
 - [49] Filipovic P, Dovic D, Ranilovic B, Horvat I. Numerical and experimental approach for evaluation of thermal performance of a polymer solar collector. *Renew Sustain Energy Rev* 2019;112(9):127–39.
 - [50] Tagliafico LA, Scarpa F, De Rosa M. Dynamic thermal models and CFD analysis for flat-plate thermal solar collectors-A review. *Renew Sustain Energy Rev* 2014;30(2):526–37.
 - [51] Alfaro-Ayala JA, Martinez-Rodriguez G, Picon-Nunez M, Uribe-Ramirez AR, Gallegos-Munoz A. Numerical study of a low temperature water-in-glass evacuated tube solar collector. *Energy Convers Manag* 2015;94(4):472–81.
 - [52] Wang KJ, Qi Xx, Liu Hd. A comparison of day-ahead photovoltaic power forecasting models based on deep learning neural network. *Appl Energy* 2019;251(10):1–14. Article 113315.
 - [53] Dong N, Chang J-F, Wu Ai-G, Gao Zh-K. A novel convolutional neural network framework based solar irradiance prediction method. *Electrical Power and Energy Systems* 2020;114(1):1–19. Article 105411.
 - [54] Heo J, Jung J, Kim B, Han S. Digital elevation model-based convolutional neural network modeling for searching of high solar energy regions. *Appl Energy* 2020;262(3):1–13. Article 114588.
 - [55] Lu Xy, Lin Pj, Cheng Shy, Lin Yh, Chen Zhc, Wu Lj, Zheng Q. Fault diagnosis for photovoltaic array based on convolutional neural network and electrical time series graph. *Energy Convers Manag* 2019;196(9):950–65.
 - [56] Herraiz AH, Marugan AP, Marquez FPG. Photovoltaic plant condition monitoring using thermal images analysis by a convolutional neural network-based structure. *Renew Energy* 2020;153(6):334–48.
 - [57] Wang KJ, Qi Xx, Liu Hd. Photovoltaic power forecasting based LSTM-Convolutional network. *Energy* 2019;189(12):1–11. Article 116225.
 - [58] Sahin M, Kaya Y, Uyar M. Comparison of ANN and MLR models for estimating solar radiation in Turkey using NOAA/AVHRR data. *Adv Space Res* 2013;51(3):891–904. Issue 5.
 - [59] Wang Zh, Wang F, Su Sh. Solar irradiance short-term prediction model based on BP neural network. *Energy Procedia* 2011;12(9):488–94.
 - [60] Liu Ly, Liu Dr, Sun Q, Li Hl, Wennersten R. Forecasting power output of photovoltaic system using a BP network method. *Energy Procedia* 2017;142(8):780–6.
 - [61] Ahmed R, Sreeram V, Mishra Y, Arif MD. A review and evaluation of the state-

- of-the-art in PV solar power forecasting: techniques and optimization. *Renew Sustain Energy Rev* 2020;124. Article 109792.
- [62] Feng C, Zhang J, SolarNet. A sky image-based deep convolutional neural network for intra-hour solar forecasting. *Sol Energy* 2020;204(7):71–8.
- [63] Hu Qh, Zhang Rj, Zhou Yc. Transfer learning for short-term wind speed prediction with deep neural networks. *Renew Energy* 2016;85(1):83–95.
- [64] Qureshi AS, Khan A, Zameer A, Usman A. Wind power prediction using deep neural network based meta regression and transfer learning. *Appl Soft Comput* 2017;58(9):742–55.
- [65] Elsheikh AH, Sharshir SW, Abd Elaziz M, Kabeel AE. Modeling of solar energy systems using artificial neural network: a comprehensive review. *Sol Energy* 2019;180(3):622–39.
- [66] Cancer M, Gedik E, Kecebas A. Investigation on thermal performance calculation of two type solar air collectors using artificial neural network. *Expert Syst Appl* 2011;38(3):1668–74.
- [67] Benli H. Determination of thermal performance calculation of two different types solar air collectors with the use of artificial neural networks. *Int J Heat Mass Tran* 2013;60(5):1–7.
- [68] Dikmen E, Ayaz M, Ezen HS, Kucuksille EU, Sahin AS. Estimation and optimization of thermal performance of evacuated tube solar collector system. *Heat Mass Tran* 2014;50(5):711–9.
- [69] Esen H, Ozgen F, Esen M, Sengur A. Artificial network and wavelet neural network approaches for modelling of a solar air heater. *Expert Syst Appl* 2009;36(10):11240–8.
- [70] Xie H, Liu L, Ma F, Fan H. Performance prediction of solar collectors using artificial neural networks. In: *Proceeding of the international conference on artificial intelligence and computational intelligence*; 2009. p. 573–6.
- [71] Varol Y, Koca A, Oztop HF, Avci E. Forecasting of thermal energy storage performance of Phase Change Material in a solar collector using soft computing techniques. *Expert Syst Appl* 2010;37(4):2724–32.
- [72] Ghritlahre HK, Prasad RK. Prediction of thermal performance of unidirectional flow porous bed solar air heater with optimal training function using Artificial Neural Network. *Energy Procedia* 2017;109(3):369–76.
- [73] Diez FJ, Navas-Gracia LM, Martinez-Rodriguez A, Correa-Guimaraes A, Chico-Santamarta L. Modelling of a flat-plate solar collector using artificial neural networks for different working fluid (water) flow rates. *Sol Energy* 2019;188(8):1320–31.
- [74] Liang RB, Ma LD, Zhang LD, Zhao D. Theoretical and experimental investigation of the filled-type evacuated tube solar collector with U tube. *Sol Energy* 2011;85(9):1735–44.
- [75] Khatib T, Mohamed A, Sopian K. A review of solar energy modeling techniques. *Renew Sustain Energy Rev* 2012;16(6):2863–9.